

A Machine-Learning Bond-Order Potential for Exploring the Configuration Space of Carbon

Ikuma Kohata,^{1,*} Kaoru Hisama,² Keigo Otsuka,¹ and Shigeo Maruyama¹

¹*Department of Mechanical Engineering, The University of Tokyo,
7-3-1 Hongo, Bunkyo-ku, Tokyo 113-8656, Japan*

²*Research Initiative for Supra-Materials, Shinshu University,
4-17-1 Wakasato, Nagano, Nagano 380-8553, Japan*

(Dated: January 22, 2025)

Construction of transferable machine-learning interatomic potentials with a minimal number of parameters is important for their general applicability. Here, we present a machine-learning interatomic potential with the functional form of the bond-order potential for comprehensive exploration over the configuration space of carbon. The physics-based design of this potential enables robust and accurate description over a wide range of the potential energy surface with a small number of parameters. We demonstrate the versatility of this potential through validations across various tasks, including phonon dispersion calculations, global structure searches for clusters, phase diagram calculations, and enthalpy-volume mappings of local minima structures. We expect that this potential can contribute to the discovery of novel carbon materials.

I. INTRODUCTION

Because of its variety of bonding states, carbon can form various allotropes with very unique physical properties such as diamond, fullerene [1], graphene [2], and carbon nanotubes [3, 4]. These carbon allotropes are actively studied, and at the same time, the prediction of novel carbon allotropes is of great interest. In the past, computational studies based on density functional theory (DFT) have predicted new hypothetical carbon allotropes such as Z-carbon [5], M-carbon [6], bct-C4 [7], and S-carbon [8]. However, the computational cost of DFT is a bottleneck in the further comprehensive search for a large number of structures without restrictions on the system size.

Empirical interatomic potentials are computationally inexpensive methods for calculating the physical properties of materials without explicitly simulating electronic structures. Among these, bond-order potentials are a class of empirical potentials designed to model the behavior of covalently bonded elements. In bond-order potentials, the total energy of the system E_{tot} is calculated as a sum of bond energies V_{ij} assigned to bond i - j ,

$$E_{\text{tot}} = \frac{1}{2} \sum_i \sum_{j \neq i} V_{ij}, \quad (1)$$
$$V_{ij} = a_{ij} V_R(r_{ij}) - b_{ij} V_A(r_{ij}).$$

Here r_{ij} is the distance between atom i and atom j in the system. V_R and V_A are the repulsive and attractive terms of a Morse-type pair potential. a_{ij} and b_{ij} are the parameters calculated from the local environments around bond i - j to scale the coefficients for the repulsive and attractive terms, respectively. The concept of the

bond-order potential was originally proposed by Abell [9] and specifically formulated by Tersoff [10]. The functional form of the bond-order potential was designed to utilize the ability of the Morse-type potential to model universal bonding behavior, provided the coefficients are properly determined. This bond-order potential, called Tersoff potential, has been parameterized for silicon [10–12], carbon [13], and multicomponent systems of group-IV elements [14–16], and many variations have been proposed over the decades, such as the Reactive Empirical Bond-Order (REBO) potential [17–19], the Adaptive Intermolecular Reactive Empirical Bond-Order (AIREBO) potential [20], the long-range carbon bond-order potential (LCBOP) [21–24], and several modified functional forms of the Tersoff potential [25–29]. Although these bond-order potentials offer simple description and fast computation of potential energy, their limited number of parameters constrains their flexibility, thereby limiting the range of structures and properties they can accurately describe and their applicability to material discovery.

In recent years, the emergence of machine learning interatomic potentials (MLIPs) has made significant progress in computational materials science. MLIPs offer a more flexible representation of the potential energy surface, enabling the description of diverse properties and structures with a single parameter set. Carbon has been one of the main targets of MLIPs for years. In early studies, MLIPs for carbon systems were developed by Khaliullin *et al.* [30] based on the neural network (NN) representation of the potential energy surface proposed by Behler and Parrinello [31] and by Bartók *et al.* [32] based on the Gaussian Approximation Potential (GAP), demonstrating the effectiveness of MLIPs in describing the complex covalent bonding systems. Starting from these studies, many MLIPs for carbon were developed using various models, including a Behler-Parrinello type architecture [33], SchNet [34], DeePMD [35], GAP [36–39], Atomic Cluster Expansion (ACE) [40], and the spectral neighbor analysis potential (SNAP) [41]. Despite

* Contact author: kohata@photon.t.u-tokyo.ac.jp

these advances, achieving comprehensive coverage of the atomic configurations and phase diagram of carbon over a wide range of pressures with a single parameter set of the limited number of parameters remains difficult due to the vast configuration space that must be captured.

One major obstacle in describing the entire potential energy surface is the poor transferability of MLIPs; they are often inaccurate outside of the configuration space covered by the training dataset. One way to overcome this and build MLIPs with good transferability is to reduce the model complexity. This is justified by the principle of Occam’s razor [42], which states that simpler explanations or models should be preferred to more complex ones if both explain the data equally well. In practice, this involves regularizing models or reducing the number of parameters. However, constructing a simple model with good accuracy is challenging because there is generally a trade-off between accuracy and model simplicity.

In this study, motivated by these issues, we present an MLIP model that combines a machine-learned bond-order with a classical two-body energy function. This model, named Machine-Learning Bond-Order Potential (MLBOP), provides a robust and accurate description of the potential energy surface with a small number of parameters. The idea of combining the traditional potential energy function with machine-learning was previously discussed by Pun *et al.*, who developed the Physically Informed Neural Network (PINN) potential [43], an MLIP model with a combination of the bond-order potential and the machine-learned on-the-fly correction of potential parameters depending on the local environments. The PINN model was used to develop general-purpose interatomic potentials for aluminum [43, 44] and tantalum [45], and demonstrated excellent robustness in extrapolation domains. The MLBOP model proposed here adopts the philosophy of the PINN model, incorporating some modifications to enhance functionality and interpretability. In the PINN model, potential parameters are obtained by summing preoptimized global parameters with machine-learned local parameters, making all potential parameters dependent on the local environment. In contrast, the MLBOP model predetermines parameters in the repulsive and attractive two-body terms based on chemical species, training only the bond-order against local environments. This approach strictly adheres to Abell’s binding energy representation, while improving interpretability and simplifying both the model structure and the training process. Furthermore, the MLBOP model incorporates a dispersion energy term expressed as an analytical function to enhance its applicability to systems where van der Waals interactions play important roles, such as layered materials.

Here we use this model to develop a general-purpose MLIP for carbon that correctly captures the continuity and smoothness of the potential energy surface over a wide range compared to other reported MLIPs. In section II, we show the formalism and parameter optimization protocol of MLBOP. In section III, we test the ro-

bustness of MLBOP by training it on several training datasets and checking the potential energy curves calculated with MLBOP. In section IV, we describe the dataset construction and training results of the general-purpose MLBOP for carbon. In section V, we evaluate MLBOP on basic physical properties of several systems, including crystal, defect, surface, liquid, and amorphous structures, and then assess the applicability of MLBOP to more advanced tasks, such as global structure searches for clusters, phase diagram calculations, and enthalpy-volume mapping of the local minima structures. Finally, in section VI, we summarize this work.

II. METHOD

A. Formulation of MLBOP

In the MLBOP model, the potential energy of the system E_{tot} is calculated as a sum of the bond energy E_{bond} and the dispersion energy E_{disp} :

$$E_{\text{tot}} = E_{\text{bond}} + E_{\text{disp}}. \quad (2)$$

The form of E_{bond} can be written as

$$E_{\text{bond}} = \frac{1}{2} \sum_i \sum_{j \neq i} [a_{ij} V_R(r_{ij}) - b_{ij} V_A(r_{ij})], \quad (3)$$

where r_{ij} , $V_R(r_{ij})$, and $V_A(r_{ij})$ are the interatomic distance between atom i and atom j , the repulsive energy shown in Eq.4, and the attractive energy shown in Eq.5, respectively. The two-body terms $V_R(r_{ij})$ and $V_A(r_{ij})$ depend only on the bond length, while the bond-orders a_{ij} and b_{ij} depend on the local environment around bond i - j . The forms of the repulsive energy V_R and the attractive energy V_A can be written as

$$V_R(r_{ij}) = f_{c1}(r_{ij}) \left(1 + \frac{Q}{r_{ij}} \right) \sum_n^3 A_n \exp(-\alpha_n r_{ij}), \quad (4)$$

and

$$V_A(r_{ij}) = f_{c1}(r_{ij}) \sum_n^3 B_n \exp(-\beta_n r_{ij}), \quad (5)$$

where f_{c1} is the cutoff function. Q , A_n , α_n , B_n , and β_n are the trainable parameters. The parameters of a_{ij} and b_{ij} are calculated as follows:

$$a_{ij} = \sigma(\phi_R(\zeta_{ij}) - \phi_R(\mathbf{0})), \quad (6)$$

$$b_{ij} = \sigma(\phi_A(\zeta_{ij}) - \phi_A(\mathbf{0})), \quad (7)$$

$$\zeta_{ij} = \sum_{k \neq i, j} f_{c2}(r_{ik}) \phi_M(r_{ij}, r_{ik}, \cos \theta_{ijk}), \quad (8)$$

where θ_{ijk} is the angle between bond i - j and i - k . f_{c2} is the cutoff function. ϕ_R , ϕ_A , and ϕ_M are the operations by multilayer perceptrons (MLPs). The output of ϕ_R

and ϕ_A is a scalar value, while ϕ_M outputs a vector. ζ_{ij} is the bond-embedded feature vector describing the local environment around bond i - j . σ is the softplus function

$$\sigma(x) = \frac{1}{\beta} \ln(1 + \exp(\beta x)) \quad (9)$$

with $\beta = \ln(2)$. The tanh activation function is applied for the hidden layers in ϕ_R , ϕ_A , and ϕ_M and the output layer in ϕ_M . To obtain a_{ij} and b_{ij} , $\phi_R(\zeta_{ij})$ and $\phi_A(\zeta_{ij})$ are shifted by $\phi_R(\mathbf{0})$ and $\phi_A(\mathbf{0})$ and then scaled by the softplus function $\sigma(x)$ to ensure that a_{ij} and b_{ij} are positive and $a_{ij} = 1$ and $b_{ij} = 1$ at $\zeta_{ij} = \mathbf{0}$, so that the energy of an isolated dimer is fixed to the two-body energy $V_R(r) - V_A(r)$. The cutoff function f_{c1} and f_{c2} are calculated as

$$f_{c1,2}(r) = \left[\frac{\tanh\{B_{c1,2}(1 - r/R_c)\}}{\tanh(B_{c1,2})} \right]^3 \quad (r < R_c), \quad (10)$$

where R_c is the cutoff distance and $B_{c1,2}$ are the trainable parameters, which have different values for f_{c1} and f_{c2} . The cutoff functions and their first and second derivative vanish at the cutoff distance R_c .

The dispersion energy term E_{disp} is calculated based on the Grimme's DFT-D3 method [46] with the Becke-Johnson damping function [47], and can be written as

$$E_{\text{disp}} = -\frac{1}{2} \sum_i \sum_{j \neq i} \left(\frac{s_6 C_{6ij}}{r_{ij}^6 + f_d(R_0)^6} + \frac{s_8 C_{8ij}}{r_{ij}^8 + f_d(R_0)^8} \right) \quad (11)$$

with

$$f_d(R_0) = a_1 R_0 + a_2. \quad (12)$$

Here s_6 , s_8 , a_1 , and a_2 are preoptimized parameters depending on the exchange-correlation functional, R_0 is a preoptimized parameter depending on the elements of atom i and atom j . C_{6ij} and C_{8ij} are the dispersion coefficients calculated from the coordination numbers around atom i and atom j .

In this work, the hyperparameters are as follows. The cutoff length R_c is set to 4.0 Å. The size of the vector ζ_{ij} is set to 20. ϕ_R and ϕ_A consist of two hidden layers, each containing 20 neurons, with their overall network structure represented as 20-20-20-1. ϕ_M has two hidden layers with 5 and 10 neurons, respectively, with its structure denoted as 3-5-10-20. The cutoff distances for E_{disp} are set to 9.0 Å for the pair interaction between atom i and j and 6.0 Å for the coordination number calculation.

B. Protocol for parameter optimization

In order to train MLBOP, we optimize an absolute combined loss function

$$L(\mathbf{w}) = \rho \sum_{i=1}^N |(E_i - gn_i) - (\hat{E}_i(\mathbf{w}) - \hat{g}(\mathbf{w})n_i)| + \sum_{i=1}^N \left(\frac{1}{3n_i} \sum_{j=1}^{n_i} \|\mathbf{F}_{i,j} - \hat{\mathbf{F}}_{i,j}(\mathbf{w})\| \right) \quad (13)$$

where \mathbf{w} represents the trainable parameters, N is the mini-batch size, i indexes each structure, and n_i denotes the number of atoms in structure i . ρ is the energy loss weight. E_i and $\mathbf{F}_{i,j}$ denote the reference DFT energy and forces, while \hat{E}_i and $\hat{\mathbf{F}}_{i,j}$ represent the predicted energy and forces. The terms g and \hat{g} correspond to the per-atom energy of a ground-state structure calculated with DFT and MLBOP, respectively. These terms are added to the loss function to compensate the energy difference coming from the zero-point energy.

The two-body and three-body parameters in E_{bond} are trained in separate stages. The two-body parameters in V_R and V_A are trained on the potential energy vs bond length curve of an isolated dimer. The three-body parameters in a_{ij} and b_{ij} are then trained on the training dataset, while the two-body parameters are fixed. The weights in the MLPs are stochastically initialized using Kaiming's method [48], and the biases are initialized to zero. The parameter optimization is performed by the mini-batch stochastic gradient descent using the ADAM optimizer [49]. The energy loss weight ρ is set to 0.1. The mini-batch size is set to 4. The initial learning rate is set to 1.0×10^{-3} and reduced to 10% each time a loss shows no improvement for 10 epochs. The parameter optimization is continued until the learning rate reaches 1.0×10^{-7} .

III. MODEL ROBUSTNESS ON POTENTIAL ENERGY SURFACES

To test the model robustness in describing potential energy surfaces, we trained MLBOP on three toy datasets of carbon, each containing 400 diamond, graphene, and simple cubic (sc) structures with lattice constants ranging from 90% to 110% of their equilibrium values and with random atomic displacements up to 0.2 Å. Each structure in the diamond, graphene, and sc datasets has 64, 50, and 64 atoms, respectively. An isolated atom was also added to each dataset to enable the models to learn the cohesive energy. To obtain the reference DFT energies, we used the the generalized gradient approximation with the Perdew-Burke-Ernzerhof (PBE) functional [50, 51] implemented in Vienna ab initio simulation package (VASP) [52–55]. For comparison, we also trained DeePMD [56] and ACE [57] on the same datasets

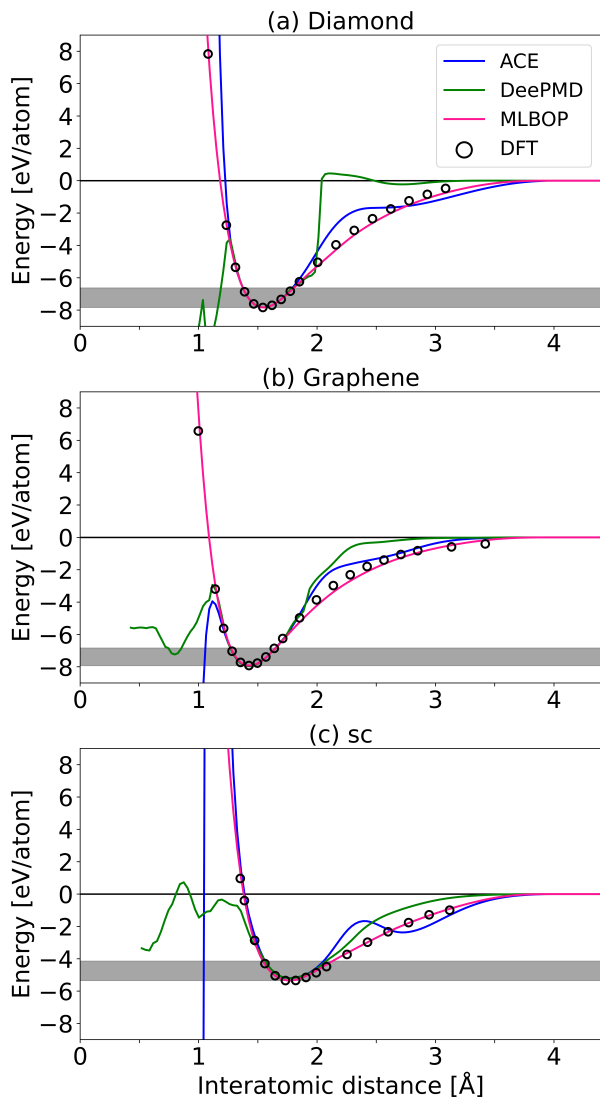


FIG. 1. Cohesive energy vs nearest-neighbor interatomic distance curves for (a) diamond, (b) graphene, and (c) sc, calculated with MLBOP, DeepMD, ACE trained on the toy datasets, and DFT (PBE). The dispersion energy term in MLBOP was omitted for comparison with the PBE energies. The gray regions indicate the per-atom energy range covered by the training datasets.

using DeePMD-kit [58] and pacemaker [59], respectively. For both models, the cutoff distance was set to 4.0 Å. ACE was regularized with an L1 parameter of 10^{-5} . Figure 1 shows the cohesive energy vs nearest-neighbor distance curves of graphene, diamond, and sc calculated with DFT, DeePMD, ACE, and MLBOP trained on each dataset. Outside the energy range covered by the training datasets, DeePMD and ACE show a discrepancy from the DFT. On the other hand, MLBOP gives a good fit to the DFT while preserving the shape of the potential energy curve derived from the Morse-type two-body function in both the interpolation and extrapolation domains.

For further testing, we trained MLBOP on the dataset used to parametrize ACE for carbon (C-ACE) [40], which includes 17293 structures with various local environments. The RMSEs of MLBOP were 136 meV/atom for energy and 0.655 eV/Å for force, which are comparable to those of C-ACE (166 meV/atom and 0.689 eV/Å). Figure 2 shows the cohesive energy vs the nearest neighbor interatomic distance curves calculated with DFT, C-ACE, and MLBOP for the first to fifteenth most unstable crystals listed in the Samara Carbon Allotrope Database (SACADA) [60] as of September 2, 2024: utb (#32 in SACADA), bcc (#8), K (#51), TY-carbon (#34), T-II carbon (#35), J (#117), fcc-C10 (#152), K6 carbon (#12), I (#135), L-carbon (#128), T-carbon (#33), supercubane C80 (#42), supercubane C96 (#43), 6(3)2-27a (#106), and Y-II carbon (#4). Compared to C-ACE, MLBOP accurately reproduced the potential energy curve with excellent smoothness over a wide range for all tested structures.

IV. TRAINING A GENERAL-PURPOSE MLBOP FOR CARBON

A. Building a training dataset

In order to develop an interatomic potential for general purposes, the training dataset structures should cover as wide a range of the potential energy surface as possible. To achieve this, we collected structures with several categories: crystal, cluster, disordered, and random structure. The crystal structures were generated by giving random atomic displacements and cell deformations to common crystal structures: graphene, graphite, nanotubes, diamond, sc, body-centered cubic (bcc), face-centered cubic (fcc), and bc8. The crystal dataset structures also include defective structures generated by randomly removing atoms or rotating bonds, and surface structures with various surface orientations. The cluster dataset structures were generated by randomly displacing atoms in linear chains and cyclic molecules with 3-12 atoms, and fullerenes with 20-80 atoms. The disordered and random dataset structures were generated by iterative and somewhat *ad hoc* expansion of the database using molecular dynamics (MD) simulation and random structure searching (RSS) [61] performed with classical interatomic potentials and MLBOP under development. The disordered structures were sampled from MD simulations at 300-10000 K starting from random structures with various densities. The random structures were obtained from the random structure search at external pressures of 0-2500 GPa using unit cells with 8-16 atoms. The resulting database contains 75332 structures and 3747903 local environments. Among the dataset structures, randomly chosen 52669 structures were used as the training dataset, the remaining structures were used as the testing dataset. The contents of the training and testing dataset are summarized in Table I and Table II, respectively.

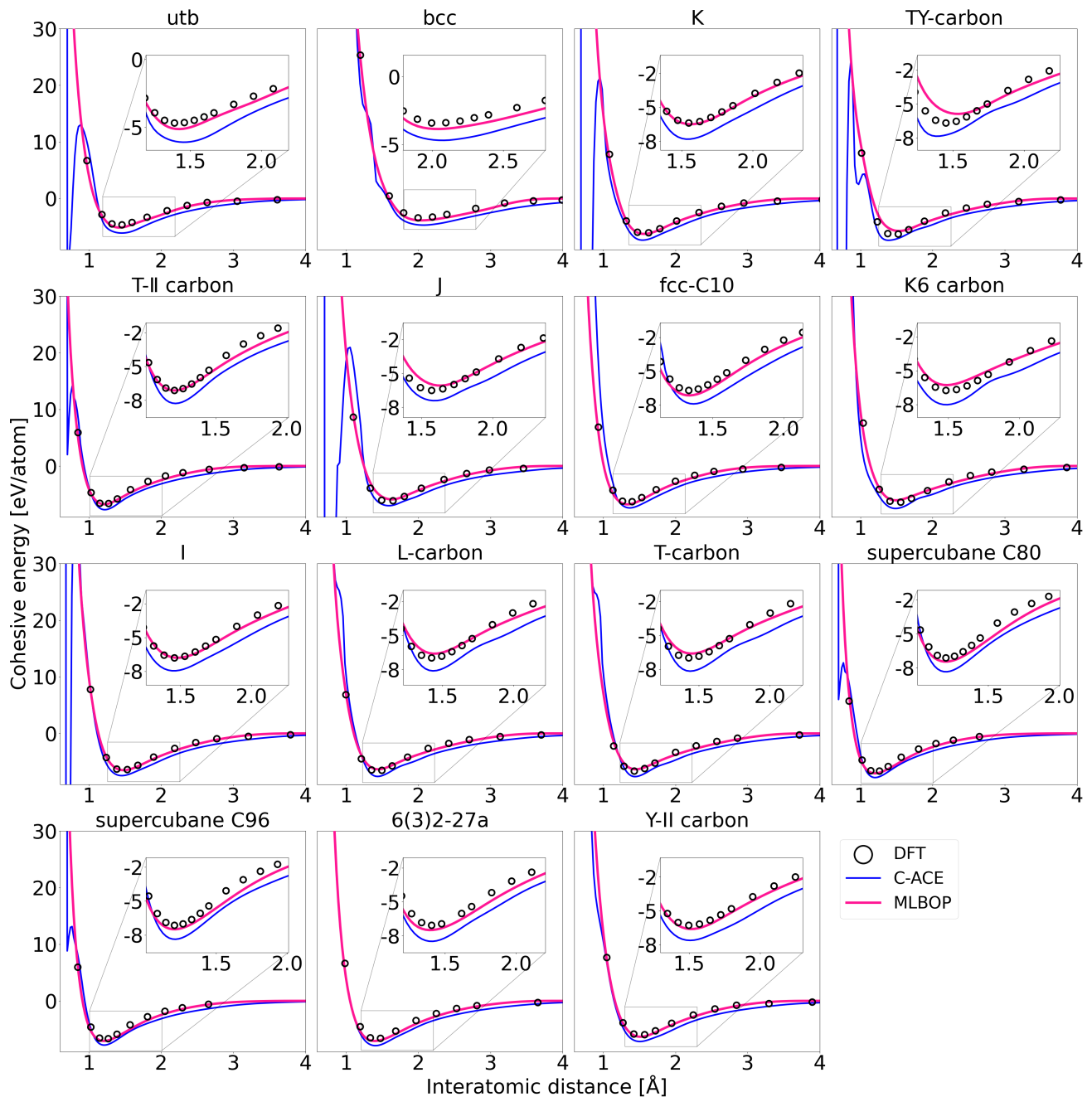


FIG. 2. Cohesive energy vs nearest-neighbor interatomic distance curves for the unstable crystals in the SACADA database, calculated with DFT (PBE), C-ACE, and MLBOP trained on the C-ACE dataset. The dispersion energy terms in MLBOP and C-ACE were omitted for comparison with the PBE energies. The boxes on the top right in each panel are magnified views of the low-energy regions.

To obtain the reference energies and forces, the spin-polarized DFT calculations were performed using the generalized gradient approximation with the PBE functional [50, 51] and the projector-augmented wave (PAW) method [62] implemented in VASP [52–55]. The PREC setting in VASP, which determines the energy cutoff and the fast Fourier transform grids, was set to Accurate, leading to a 400 eV cutoff. A Γ -centered k-point mesh

with 0.033 \AA^{-1} spacing was used for the periodic directions, and one k-point for the vacuum directions. The Gaussian smearing was used with a 0.05 eV smearing width. The convergence criterion for the electronic self-consistent loop was set to 10^{-4} eV. In the following sections, unless otherwise noted, the settings for DFT calculations are the same as those described here.

TABLE I. Contents of our training dataset. The first column is the structure type. The second column is the number of structures. The third column is the number of distinct local environments.

Structure type	No. structures	No. environments
<i>sp</i> ² structure		
Monolayer graphene	4791	499388
AA-bilayer graphene	560	35840
AB-bilayer graphene	560	35840
AA-graphite	560	35840
AB-graphite	560	35840
Nanotube	2779	268096
Diamond	5052	743623
General crystal		
bc8	1061	135808
sc	1112	139000
bcc	840	107520
fcc	840	90720
Cluster		
Ring	2519	18440
Chain	4200	15120
Fullerene	910	33662
Disordered	9340	340136
Random	16985	164720
Total	52669	2699593

TABLE II. Contents of our testing dataset. The columns are the same as in Table I.

Structure type	No. structure	No. environment
<i>sp</i> ² structure		
Monolayer graphene	2184	220950
AA-bilayer graphene	240	15360
AB-bilayer graphene	240	15360
AA-graphite	240	15360
AB-graphite	240	15360
Nanotube	1190	115544
Diamond	1401	247121
General crystal		
bc8	237	30336
sc	240	30000
bcc	360	46080
fcc	360	38880
Cluster		
Ring	1079	7934
Chain	1800	6480
Fullerene	390	14338
Disordered	4003	146151
Random	8459	83056
Total	22663	1048310

B. Training results

As a result of the parameter optimization of MLBOP on our training dataset, the mean absolute errors (MAEs) of energies and atomic forces are 27.81 meV/atom and 0.395 eV/Å for the training dataset, 29.76 meV/atom and

0.387 eV/Å for the testing dataset. Figure 3 compares the energies and forces between DFT and MLBOP for the testing dataset. The MLBOP energies and forces are in good agreement with DFT across a wide range.

For comparison, we also trained other MLIP models, DeePMD [56], SchNet [63] and ACE [57], on our training dataset. For the training of DeePMD, we used DeePMD-kit [58]. The se_e2_a descriptor was used to represent the local environment. The cutoff distance was set to 4.0 Å to define the local environment, with a smoothing cutoff of 0.5 Å. The embedding net consists of 3 hidden layers, each having 25, 50, and 100 neurons. The number of axis neurons is set to 16. The fitting net has 3 hidden layers with 256 neurons each. The GELU activation function [64] was applied for each hidden layer in the embedding and fitting net. The energy loss and force loss weights were set to 0.1 and 1.0, respectively, and remained constant throughout the training. The training was performed using the ADAM optimizer for 20000000 batches with a batch size of 4. The initial learning rate was set to 10⁻³ and exponentially decayed to 10⁻⁶ by the end of the training.

For the training of SchNet, we used the implementation in the documentation of PyTorch Geometric [65] with modifications for the force calculation in periodic boundary conditions. The cutoff distance was set to 4.0 Å for each interaction block. The number of interaction blocks was 3. The number of feature dimensions, filters, and Gaussians were set to 128, 128, and 40, respectively. The loss function was calculated as

$$L(\mathbf{w}) = \rho \sum_{i=1}^N |E_i - \hat{E}_i(\mathbf{w})| + \sum_{i=1}^N \left(\frac{1}{3n_i} \sum_{j=1}^{n_i} \|\mathbf{F}_{i,j} - \hat{\mathbf{F}}_{i,j}(\mathbf{w})\| \right) \quad (14)$$

with $\rho = 0.1$. The training was performed with the mini-batch stochastic gradient descent using the ADAM optimizer with a mini-batch size of 4. The learning rate was initially set to 1.0×10^{-3} , which exponentially decayed every epochs with a decaying rate of 0.99. The training was continued until the learning rate reached 1.0×10^{-6} .

For the training of ACE, we used pacemaker [59]. The cutoff distance was set to 4.0 Å, and 603 basis functions up to the fifth body order were applied. The loss weight parameter κ was set to 0.6. The loss function was calculated only from energy and force losses without regularization, and the uniform weighting policy was used to assign equal weights to all structures. Training was performed using the BFGS algorithm with the ladder basis extension. In the last ladder step, the training was continued until it was automatically stopped by the early stopping function. For the early stopping, the minimal relative change in the train loss per iteration was set to 1.0×10^{-5} with a patience of 200 steps.

Table III compares the MAEs of energy and force for the training and testing datasets. The results demon-

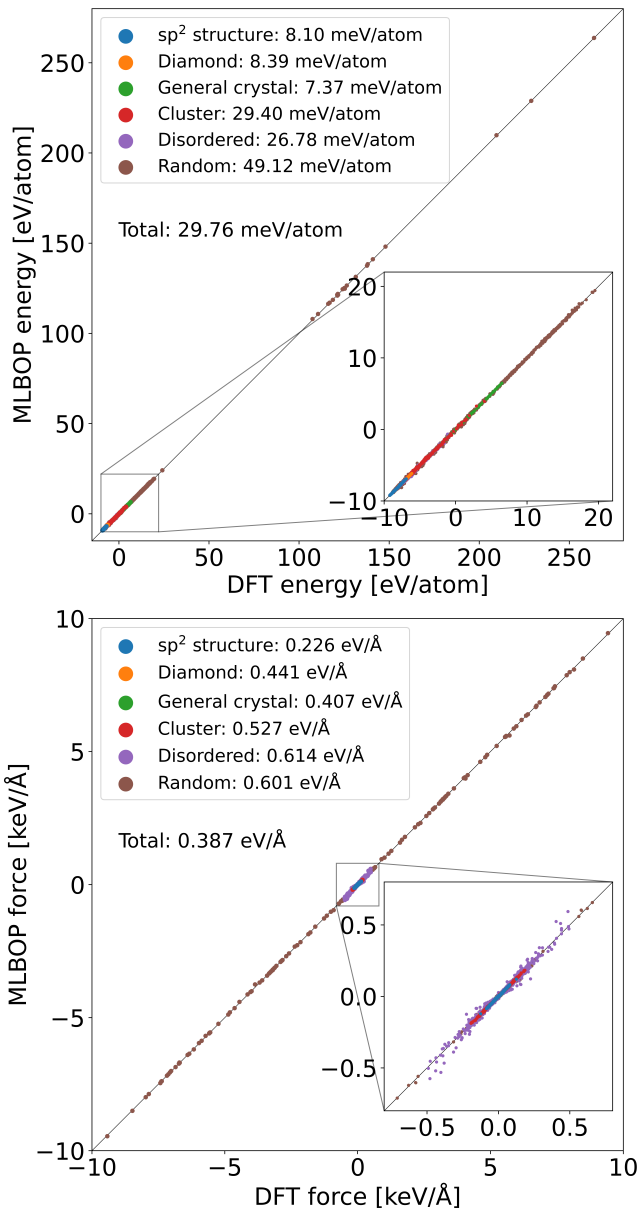


FIG. 3. Comparison between DFT and MLBOP for the testing dataset. Top: Energy. Bottom: Force. The colors of the circles represent the type of the dataset structure. The MLBOP energies are adjusted by a constant shift to match the DFT energies. Insets show magnified views for the low energy regions. The values in the panels are the MAEs for each structure type.

strate that MLBOP achieves comparable or better accuracy than MLIP models with a larger number of parameters.

V. VALIDATION

In developing interatomic potentials, regression metrics on a given test dataset are insufficient to measure

TABLE III. Model comparison of the number of parameters and MAEs of energies E and forces F for the training and testing datasets. The MAEs are given in meV/atom for energy and eV/Å for force.

Model	No. parameters	E_{train}	F_{train}	E_{test}	F_{test}
DeePMD	550260	89.41	0.584	92.78	0.581
SchNet	221953	25.54	0.492	31.42	0.510
ACE	3002	145.9	0.374	140.3	0.399
MLBOP	2019	27.81	0.395	29.76	0.387

performance. To confirm the applicability of an interatomic potential, it is essential to evaluate it from multiple perspectives. In this section, we validate the MLBOP developed in section IV by checking its accuracy on various physical properties.

A. Crystal

As a first test, we calculated the cohesive energy vs the nearest neighbor interatomic distance curves using DFT and MLBOP for dimer, monolayer graphene, diamond, sc, bc8, bcc, and fcc, as shown in the top in Figure 4. The cohesive energy curves calculated with MLBOP are in good agreement with the DFT and have good smoothness over a wide range of interatomic distances. We also calculated the binding energy of AA- and AB-stacked graphite and bilayer graphene as a function of the interlayer distance using DFT and MLBOP, as shown in the bottom in Figure 4, and the binding energy curves calculated with MLBOP also agree with DFT.

In addition, for unbiased validation, the cohesive energy curves of the first to fifteenth most unstable crystals in the SACADA database, which are not explicitly included in the training dataset except for bcc, were computed again. Figure 5 shows the cohesive energy curves calculated using DFT (PBE-D3), MLBOP, GAP-20 [37, 38], C-SNAP [41], and C-ACE [40]. The MLBOP curves have no unphysical local minima and good smoothness in agreement with the DFT over a wider range of energy curves compared to other reported MLIPs.

B. Defect

We evaluate MLBOP by calculating defect formation energies for various defects in monolayer graphene, diamond, (5,5) and (9,0) nanotubes. The defect formation energy E_f is defined as

$$E_f = E_d - N\mu, \quad (15)$$

where E_d is the total energy of the defective structure, N is the number of atoms in the defective structure, and μ is the per-atom energy of the defect-free structure.

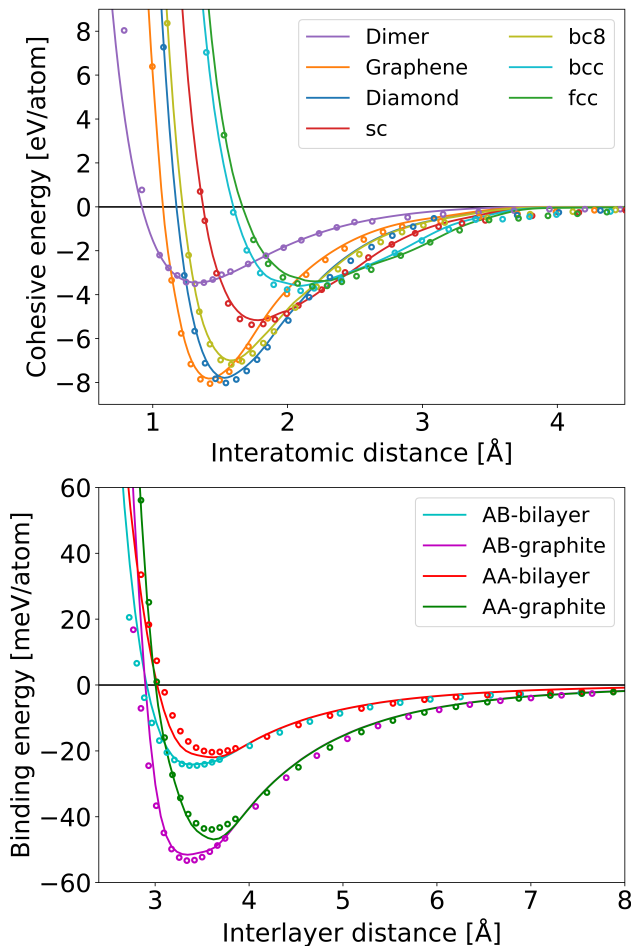


FIG. 4. Top: Cohesive energy vs nearest-neighbor interatomic distance curves for dimer, monolayer graphene, diamond, sc, bc8, bcc, and fcc calculated with MLBOP and DFT (PBE-D3). Bottom: Binding energy vs interlayer distance curves for AB- and AA-stacked graphite and bilayer graphene calculated with MLBOP and DFT (PBE-D3). The lines indicate the MLBOP energies and the circles indicate the DFT energies.

Each defective structure was generated with a supercell of $(11 \times 11 \times 1)$ with 242 atoms for graphene, $(3 \times 3 \times 3)$ with 216 atoms for diamond, supercells with 180 atoms and 178 atoms for (5,5) and (9,0) nanotubes, respectively. The defect-free structures were relaxed with respect to the atomic configurations and cell parameters. The defective structures were generated by manipulating atoms in the supercell of the defect-free structure, followed by relaxation to local minima while keeping cell parameters fixed. The structural optimizations and defect formation energy calculations were performed using DFT, MLBOP, the second generation REBO potential (REBO-II) [19], GAP-20, C-SNAP, and C-ACE. The DFT calculations were performed using two exchange correlation functionals, PBE-D3 and optB88 [66–69]. Although some defect formation energies have been previously reported, all values were recalculated to ensure consistency in compu-

tational conditions and protocols. For the DFT calculations, the convergence criteria for the electronic self-consistent loop and the ionic relaxation loop were set to 10^{-6} and 10^{-5} eV, respectively. For the interatomic potentials, the structural optimizations were performed using LAMMPS [70], and the convergence criteria of energy and force were set to 10^{-10} eV and 10^{-8} eV/Å, respectively. Table IV lists the calculated defect formation energies. MLBOP predicted the defect formation energies with accuracies comparable to or better than other MLIPs.

C. Surface

We evaluate MLBOP by calculating surface energies for diamonds with various surface orientations. The surface energy E_{surf} is calculated as

$$E_{\text{surf}} = \frac{E_{\text{slab}} - N\mu}{2A}, \quad (16)$$

where E_{slab} is the total energy of the surface slab, N is the number of atoms in the slab, μ is the per-atom energy of the bulk structure, and A is the slab surface area. We calculated the surface energies of both ideal and relaxed surfaces with (100), (111), and (110) orientations, as well as the (2×1) -reconstructed surfaces of (100) and (111), called Pandey-chain reconstruction. The reconstructed surfaces were obtained from DFT-MD simulations of diamond slabs, followed by the optimization of atomic configurations to local energy minima using the other interatomic potentials tested. The settings for the structural optimizations were the same as those used for the defect formation energy calculations. Table V shows the surface energies calculated with DFT (PBE-D3, optB88, and B3LYP [71–73]), MLBOP, REBO-II, GAP-20, C-SNAP, and C-ACE. MLBOP achieves a similar level of accuracy in predicting the surface energies as GAP-20 and C-ACE. We also calculated the edge energies of graphene and carbon nanotubes with different edge orientations: zigzag and armchair. The edge energy E_{edge} is defined as

$$E_{\text{edge}} = \frac{E_{\text{cut}} - N\mu}{2L}, \quad (17)$$

where E_{cut} is the total energy of the structure with the exposed edge, N is the number of atoms in this structure, μ is the per-atom energy of the edge-free structure, and L is the length of the edge. Table V shows the zigzag edge energy of graphene and a (9,0) nanotube and the armchair edge energy of graphene and a (5,5) nanotube. For both graphene and nanotubes, DFT calculation predicts that the armchair edge energy is lower than the zigzag edge energy. MLBOP can reproduce this trend as can GAP-20 and C-ACE.

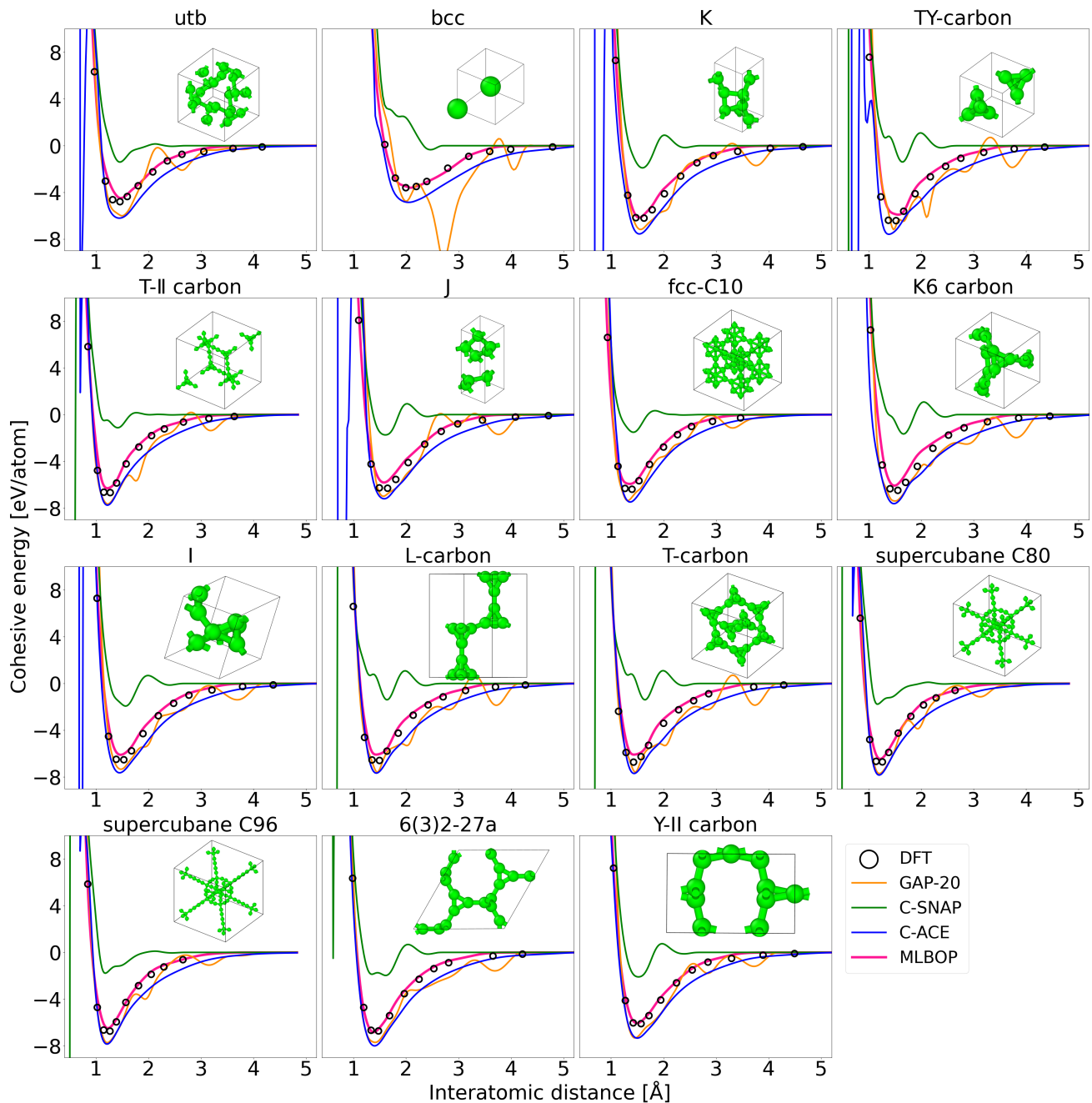


FIG. 5. Cohesive energy vs nearest-neighbor interatomic distance curves for the unstable crystals in the SACADA database, calculated with DFT (PBE-D3), GAP-20, C-SNAP, C-ACE, and MLBOP. The unit cells of the crystals are shown in each panel.

D. Liquid

We compared the liquid structures obtained from MD simulations using DFT, MLBOP, REBO-II, GAP-20, and C-ACE. The DFT-MD simulations were conducted with the PBE-D3 functional and a single k-point, using VASP with the PREC setting at Medium. Each MD simulation included 64 atoms at densities of 1.75, 2.44, and 3.20 g/cm³, and was run for 30 ps at 5000 K with a 2.0

fs timestep, starting with a simple cubic (sc) structure. The radial distribution function (RDF) and angular distribution function (ADF) were averaged over the last 15 ps of each simulation. Figure 6 shows the RDF and ADF at each density. These structural quantities calculated with MLBOP closely match the DFT results across all distances and angles, without spurious peaks, as are those obtained with GAP-20 and C-ACE.

TABLE IV. Formation energies of various defects in graphene, nanotubes, and diamond. The formation energies were calculated with DFT (PBE-D3 and optB88), MLBOP, REBO-II, GAP-20, C-SNAP, and C-ACE. In brackets is the percentage error from the PBE-D3 value.

	Defect formation energy [eV] (% error)						
	DFT (PBE-D3)	MLBOP	REBO-II	GAP-20	C-SNAP	C-ACE	DFT (optB88)
Graphene Stone-Wales	4.79	4.70 (2)	5.46 (14)	5.12 (7)	4.65 (3)	4.86 (1)	5.01
Graphene monovacancy	7.82	7.24 (7)	7.52 (4)	6.99 (11)	3.19 (59)	7.05 (10)	8.03
Graphene divacancy (5-8-5)	7.11	7.27 (2)	7.37 (4)	7.86 (11)	6.08 (14)	7.22 (2)	7.29
Graphene divacancy (555-777)	6.54	6.08 (7)	6.68 (2)	6.87 (5)	6.72 (3)	6.35 (3)	6.78
Graphene divacancy (5555-6-7777)	6.64	6.36 (4)	7.38 (11)	7.37 (11)	7.68 (16)	6.89 (4)	6.87
Graphene adatom	6.48	5.55 (14)	6.09 (6)	5.26 (19)	-2.04 (131)	5.29 (18)	6.40
(5,5) nanotube monovacancy	6.75	6.28 (7)	6.28 (7)	6.36 (6)	-0.41 (106)	5.67 (16)	6.73
(5,5) nanotube divacancy	4.38	3.91 (11)	5.01 (14)	4.58 (5)	-4.50 (203)	4.35 (1)	4.33
(5,5) nanotube Stone-Wales (parallel)	3.78	3.38 (11)	4.80 (27)	3.88 (3)	-5.17 (237)	3.74 (1)	3.71
(5,5) nanotube Stone-Wales (transverse)	3.12	2.66 (15)	3.67 (18)	3.06 (2)	-2.25 (172)	3.07 (2)	3.11
(9,0) nanotube monovacancy	5.54	4.92 (11)	4.90 (12)	4.92 (11)	-2.99 (154)	4.52 (18)	5.52
(9,0) nanotube divacancy	3.38	3.27 (3)	4.25 (26)	3.53 (4)	-3.54 (205)	3.42 (1)	3.39
(9,0) nanotube Stone-Wales (parallel)	2.91	2.71 (7)	3.56 (23)	2.93 (1)	-0.06 (102)	3.09 (6)	2.92
(9,0) nanotube Stone-Wales (transverse)	3.68	3.11 (16)	4.37 (19)	3.33 (10)	-3.41 (193)	3.54 (4)	3.69
Diamond monovacancy	7.01	6.70 (4)	7.17 (2)	4.28 (39)	1.48 (79)	5.73 (18)	6.55
Diamond divacancy	9.51	10.01 (5)	10.77 (13)	6.71 (29)	2.23 (77)	8.93 (6)	8.98
Diamond interstitial	11.86	10.26 (13)	10.05 (15)	7.98 (33)	8.76 (26)	8.42 (29)	11.47

TABLE V. Surface energies of diamond with different orientations calculated with DFT (PBE-D3, optB88, and B3LYP), MLBOP, REBO-II, GAP-20, C-SNAP, and C-ACE. The B3LYP values are from Ref. [74]. In brackets is the percentage error from the PBE-D3 value.

	Surface energy [eV/Å ²] (% error)							
	DFT (PBE-D3)	MLBOP	REBO-II	GAP-20	C-SNAP	C-ACE	DFT (optB88)	DFT (B3LYP)
(100) 1×1 ideal	0.579	0.634 (10)	0.727 (26)	0.641 (11)	0.221 (62)	0.590 (2)	0.557	0.582
(100) 1×1 relaxed	0.562	0.603 (7)	0.722 (29)	0.586 (4)	0.212 (62)	0.573 (2)	0.539	0.567
(100) 2×1 reconstructed	0.341	0.352 (3)	0.435 (28)	0.322 (6)	0.163 (52)	0.382 (12)	0.322	0.301
(111) 1×1 ideal	0.481	0.457 (5)	0.465 (3)	0.371 (23)	0.092 (81)	0.514 (7)	0.483	0.506
(111) 1×1 relaxed	0.423	0.411 (3)	0.423 (0)	0.263 (38)	0.084 (80)	0.405 (4)	0.422	0.403
(111) 2×1 reconstructed	0.239	0.272 (14)	0.234 (2)	0.224 (7)	0.224 (6)	0.315 (32)	0.239	0.235
(110) 1×1 ideal	0.453	0.405 (11)	0.289 (36)	0.340 (25)	0.097 (79)	0.451 (0)	0.439	0.465
(110) 1×1 relax	0.367	0.357 (3)	0.220 (40)	0.258 (30)	0.081 (78)	0.374 (2)	0.346	0.406

E. Amorphous phase

We verified MLBOP for the structure of amorphous carbon obtained by melt-quench MD simulation by comparison with the experimental data. For the melt-quench simulations, we generated sc structures with 8000 atoms at a density of 2.0 g/cm³. These structures were randomized by MD simulations at 12000 K for 4 ps, held at 8000 K for 10 ps, and then quenched to 300 K by linearly decreasing temperature at cooling rates of 10 K/ps, 100 K/ps, and 1000 K/ps. The timestep was set to 1.0 fs. Figure 7 compares the structure factor $S(q)$ of amorphous carbon obtained from the melt-quench simulations with that from the neutron diffraction of amorphous carbon film prepared by sputtering [75]. The structure of amor-

phous carbon depends on the cooling rate, with slower cooling rates yielding more stable graphitic structures. A fast cooling rate of 1000 K/ps results in the structure factor in good agreement with the neutron diffraction data, showing that MLBOP can produce a realistic amorphous structure by properly choosing a cooling rate, despite the difference in synthesis method between sputtering and melt quenching.

F. Phonons

We tested MLBOP on the phonon band structures of diamond, graphene, bc8, and sc. Phonon calculations were performed using DFT (PBE-D3), GAP-20, C-ACE,

TABLE VI. Edge energies of graphene and nanotubes calculated with DFT (PBE-D3 and optB88), MLBOP, REBO-II, GAP-20, C-SNAP, and C-ACE. In brackets is the percentage error from the PBE-D3 value.

	Edge energy [eV/Å] (% error)						DFT (optB88)
	DFT (PBE-D3)	MLBOP	REBO-II	GAP-20	C-SNAP	C-ACE	
Graphene armchair	1.04	1.03 (1)	1.09 (5)	1.11 (7)	0.47 (55)	0.94 (10)	1.02
Graphene zigzag	1.20	1.16 (4)	1.04 (14)	1.25 (3)	0.39 (68)	0.97 (20)	1.23
(5,5) nanotube armchair	0.96	1.01 (6)	1.01 (6)	1.00 (5)	0.37 (61)	0.88 (8)	0.93
(9,0) nanotube zigzag	1.18	1.15 (3)	0.96 (19)	1.04 (12)	0.29 (75)	0.93 (21)	1.20

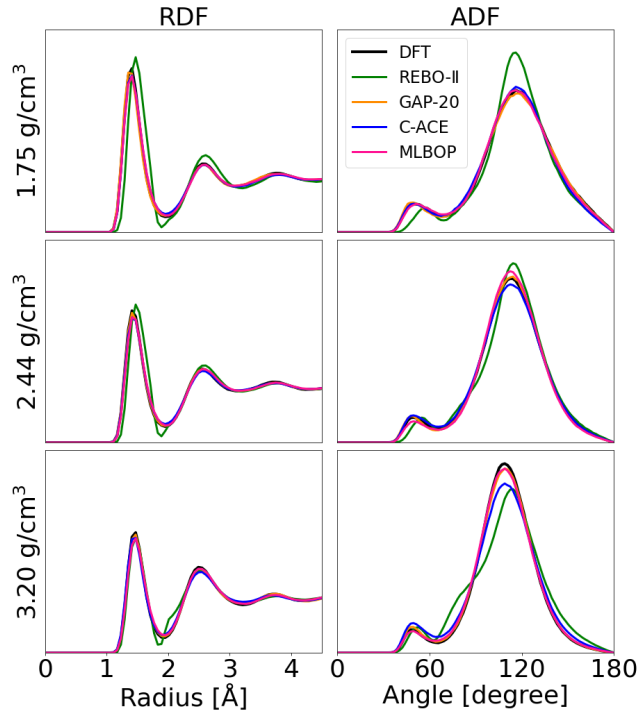


FIG. 6. RDFs and ADFs of liquid carbon with densities of 1.75 (top row), 2.44 (middle row), and 3.20 g/cm³ (bottom row) at 5000 K for DFT (PBE-D3), REBO-II, GAP-20, C-ACE, and MLBOP

and MLBOP. These calculations were carried out with phonopy [76, 77] following full structural relaxation with each method. Figure 8 shows the phonon band structures and density of states (DOS) for each structure. The phonon band structures and DOS obtained using MLBOP agree with those from DFT, as do the results from GAP-20 and C-ACE.

G. Cluster

To validate MLBOP’s ability to predict stable structures of carbon clusters, we optimized the geometries of clusters using a structural optimization method based on the genetic algorithm (GA). This approach involved

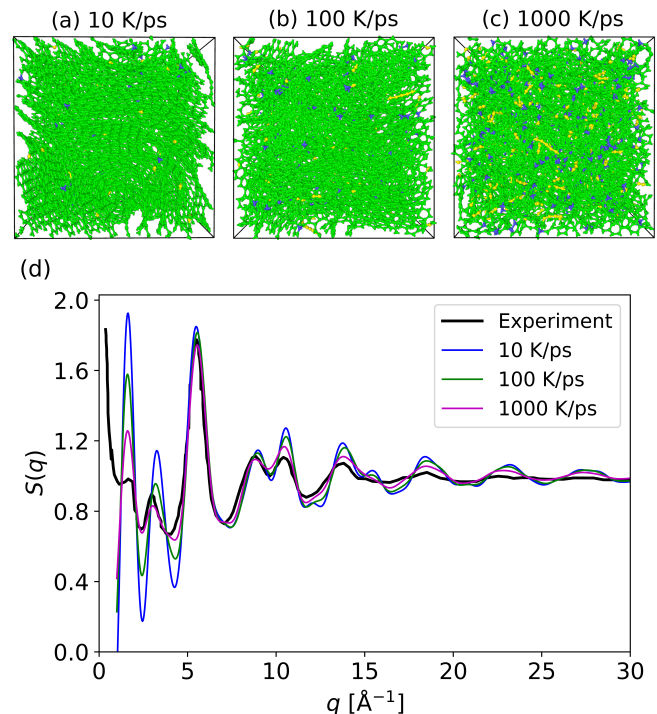


FIG. 7. Amorphous carbon with a density of 2.0 g/cm³ obtained from the melt-quench MD simulations of 8000 atoms at cooling rates of (a) 10 K/ps, (b) 100 K/ps, and (c) 1000 K/ps. The yellow, green, and blue balls represent two-, three-, and four-coordinated carbon atoms, respectively. The cutoff distance for calculating the coordination number is 1.85 Å. (d) Comparison of the structure factor $S(q)$ between the melt-quench MD simulations and the neutron diffraction of amorphous carbon with a macroscopic density of 2.0 g/cm³ [75].

mating, selection, and mutation operations on candidate structures within a population as described below.

Each candidate structure is represented by N lists of atomic coordinates \mathbf{x}_i

$$G = \{\mathbf{x}_1, \mathbf{x}_2, \dots, \mathbf{x}_N\}. \quad (18)$$

The initial population consists of eight candidate structures, each generated by randomly placing N atoms in a sphere of 6.0 Å diameter and then relaxing the atomic configurations to local minima. A child structure is pro-

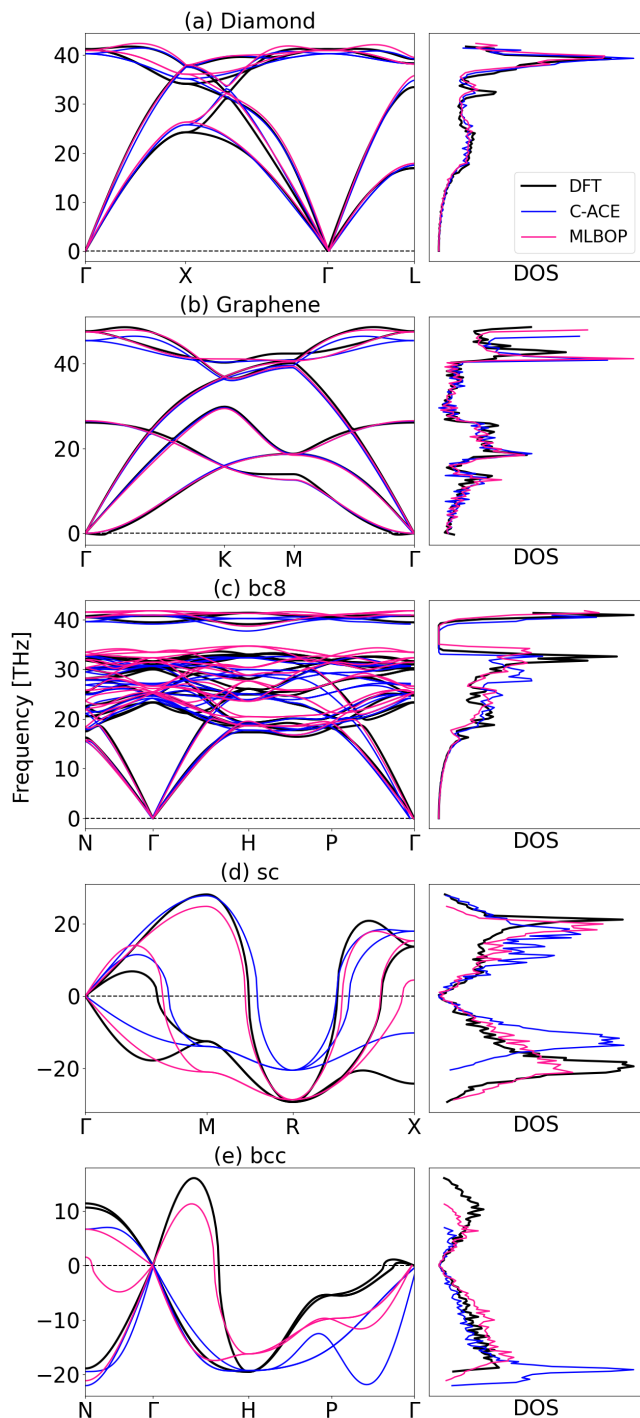


FIG. 8. Phonon band structures and DOS of (a) diamond, (b) graphene, (c) bc8, (d) sc, and (e) bcc calculated with DFT (PBE-D3), C-ACE, and MLBOP.

duced using the cut-assemble mating operation [78]. In this process, two parent structures, G and G' , are randomly selected from the population, randomly rotated, aligned so their centers of mass are at the origin, and cut along the XOY plane. A child structure, G'' , is then generated by assembling the atoms of G which lie above

the plane, and the atoms of G' which lie below the plane. If the resulting child structure does not have the correct number of atoms N , the parent clusters are translated equal distances in opposite directions, and the process is repeated. After relaxation to the local minimum, the child structure replaces another candidate in the population if its energy is lower. As the optimization progresses, the population can be dominated by candidates with similar structures, stalling further evolution. In such cases, instead of the mating operation, a mutation operation generates a new candidate as follows. First, a structure G^* is selected from the population. Then, a new candidate structure G^{**} is produced by randomly selecting a bond between two atoms within 1.8 Å in G^* , and rotating it 90 degrees about an axis passing through the center of mass of G^* and perpendicular to the bond. The new candidate structure G^{**} is relaxed and replaces a candidate in the population if it has a lower energy. The choice between mutation or mating is based on the coordination number of atoms in the population: if all atoms have the same coordination number, the mutation is performed; otherwise, mating is chosen. A cutoff distance of 1.85 Å was used to calculate the coordination number. The GA optimizations were performed for 10000 generations on different sized clusters C_N ($4 \leq N \leq 64$, N is even) using MLBOP. The energies of the GA-optimized structures were recalculated with DFT for verification.

The top in Figure 9 shows the GA-optimized structures obtained using MLBOP. The structures optimized using MLBOP exhibit diverse forms depending on the cluster size: chain for $N \leq 4$, monocyclic ring for $6 \leq N \leq 20$, and cage for $22 \leq N \leq 64$, including the buckyball structure for C_{60} . This size-dependent structural evolution from chains to rings, and eventually to cages, is consistent with previous DFT studies [79]. The bottom in Figure 9 shows the energies of the GA-optimized structures calculated with MLBOP and DFT, and the DFT energies of the DFT-relaxed structures starting from the GA-optimized structures. The DFT relaxation caused only small atomic displacements and energy differences in the GA-optimized structures obtained with MLBOP, indicating that MLBOP accurately predicts at least the local minima structures. The MLBOP energies of the cage structures are in good agreement with the DFT energies. In the DFT calculations, C_{4N} rings are less stable compared to C_{4N+2} rings due to differences in aromaticity. However, this instability is not reproduced by MLBOP; the MLBOP energy of C_{4N} rings lies between that of C_{4N-2} and C_{4N+2} . These indicate that the accuracy of MLBOP trained in this study is limited for small clusters with 20 atoms or less, suggesting room for improvement.

H. Phase diagram

To evaluate the performance of MLBOP in capturing phase behavior, we calculated the phase diagram of carbon using MLBOP at pressures from 0.02 GPa to 2500

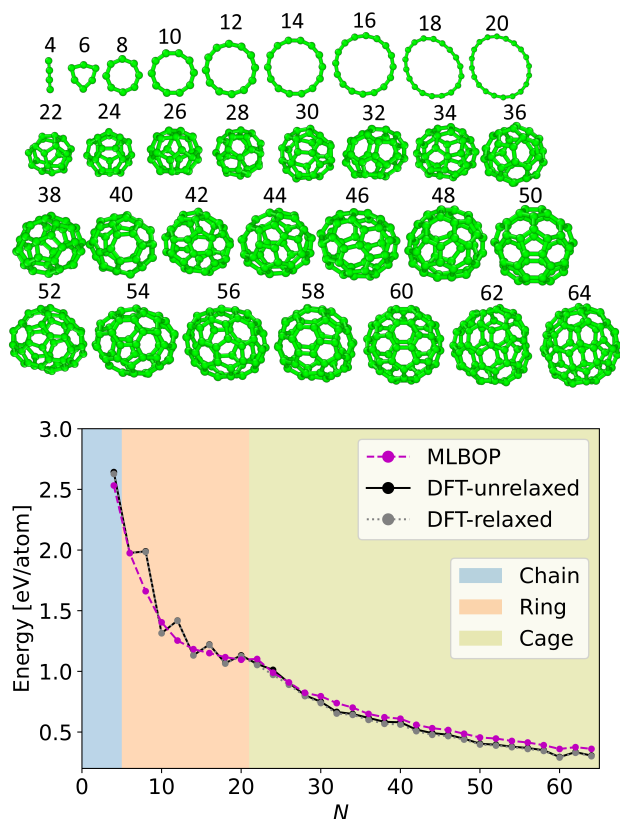


FIG. 9. Top: GA-optimized structures of C_N ($4 \leq N \leq 64$, N is even) obtained using MLBOP. Bottom: Energies (relative to monolayer graphene) of the GA-optimized structures obtained using MLBOP. The magenta and black points indicate the MLBOP and DFT (PBE-D3) energies of the GA-optimized structures, respectively. The gray points indicate the DFT energies of the DFT-relaxed structures starting from the GA-optimized structures. The blue, orange, and beige regions represent the size ranges in which C_N is a chain, monocyclic ring, and cage, respectively.

GPa. To determine the melting points of graphite, diamond, and bc8, solid-liquid two-phase simulations [80] were conducted. These simulations included 1008, 1024, and 864 atoms for graphite, diamond, and bc8, respectively, within orthogonal cells. The graphite-liquid interface was oriented perpendicular to the graphite layers, while the diamond-liquid and bc8-liquid interfaces were separated by the (100) surface. The two-phase simulations were performed using isothermal-isobaric (NPT) MD simulation for 40 ps, with a time step of 1 fs and varying temperatures in 25 K increments at each pressure. Melting points were determined as the solid-liquid equilibrium temperature. The solid-liquid phase transition was identified by monitoring the time history of the averaged Steinhardt order parameter [81]: specifically, Q_3 for the graphite-liquid system and Q_6 for the diamond- and bc8-liquid systems. To obtain the graphite-diamond and diamond-bc8 transition lines, we calculated the Gibbs free energy using phonon calculations within the quasi-

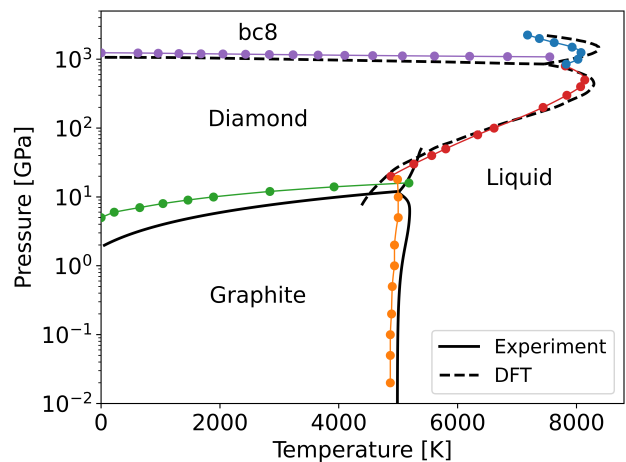


FIG. 10. Phase diagram of carbon calculated with MLBOP. The green and purple dots indicate the graphite-diamond and the diamond-bc8 transition points, respectively. The orange, red, and blue dots indicate the melting points of graphite, diamond, and bc8, respectively. The colored lines are the transition and melting lines obtained as interpolations. The phase diagrams from the experiment (solid, black) [82] and the DFT calculation (dashed, black) [83] are shown for comparison.

harmonic approximation. The transition points were determined as temperatures at which the Gibbs free energies of the two structures are equal at each pressure. The phonon calculations were performed using phonopy [76, 77]. Figure 10 compares the phase diagram calculated with MLBOP with those from experiments [82] and DFT calculations [83]. Overall, the MLBOP-calculated phase diagram shows good agreement with the DFT and experimental results. The graphite-diamond transition line obtained with MLBOP is slightly shifted above the experimental transition line. Specifically, the graphite-diamond transition point at 0 K calculated using MLBOP is 5.2 GPa, which is about 3 GPa higher than the experimental value. However, the MLBOP value is in agreement with the PBE-D3 value of 5.5 GPa, obtained using the same settings used to calculate the reference DFT energies. Thus, the shift in the graphite-diamond transition line is caused by inaccuracies in the DFT calculation method rather than fitting errors in MLBOP.

I. Enthalpy-volume map of local minima structures

As shown in Figure 5 and mentioned in Refs. [38, 84], reported MLIPs for carbon often show some spurious ground state structures, which limits their applicability to structure searching. To validate the correctness of the ground state structures predicted by MLBOP and its suitability for exploring the configuration space, we performed the RSS with applying external pressures of 0, 100, 300, 500, 800, 1000, 1500, 2000, and 2500 GPa.

For each pressure, a total of 800 structures, 400 with 8 atoms and 400 with 16 atoms in the unit cell were used as initial configurations for the RSS. These structures were generated by randomly placing atoms in a $3 \times 3 \times 3 \text{ \AA}^3$ cell with a minimum interatomic spacing of 1.1 \AA . The atomic configurations and cell geometries were optimized using MLBOP and the FIRE algorithm implemented in LAMMPS. During the optimization, the pressures in the normal (x , y , z) and shear (xz , xy , yz) directions were independently controlled, leading to a triclinic cell shape of the optimized structures. The energies of the MLBOP RSS minima structures were recomputed with DFT using the PBE-D3 functional. Figure 11 shows the enthalpies and volumes of the RSS minima calculated with MLBOP. The convex hull shapes surrounding these minima are consistent with those from DFT calculations, indicating that MLBOP accurately reproduces the relative stability of structures at the convex hull points. The ground-state structures are AB-stacked graphite at 0 GPa, diamond between 100–800 GPa, and bc8 at higher pressures in agreement with DFT results. The top panel in Figure 12 compares the energies of the MLBOP RSS minima structures between DFT (PBE-D3) and MLBOP. The bottom panel in Figure 12 compares the energy prediction on the same RSS minima structures between GAP-20, C-ACE, and MLBOP. Compared to GAP-20 and C-ACE, MLBOP accurately reproduced the DFT energies of the RSS minima structures over a wide range of pressures and achieved an accuracy of MAE 64.9 meV/atom.

We also performed the RSS using C-ACE and GAP-20 starting from the same initial structures employed in the MLBOP RSS. For C-ACE, the majority of RSS structures collapsed to extremely small volumes at pressures exceeding 300 GPa with energies significantly lower than that of graphite due to the presence of spurious local minima in dense configurations. This unphysical energy drop in the repulsive extrapolation domains is a typical behavior of the ACE model and may be modified by replacing it with a pairwise core repulsion term as described in Ref. [85]. GAP-20 produced spurious ground-state phases such as strained diamond and strained hexagonal structures at pressures above 300 GPa, consistent with the findings reported in Ref. [84]. MLBOP did not produce spurious minima structures and correctly predicted ground state phases at each pressure, demonstrating the quality of the potential energy surface and the accuracy of the structural stability in the potential energy surface over a wide pressure range.

VI. CONCLUSION

In this work, we constructed an MLIP model by combining a machine-learned bond-order with a Morse-type two-body energy function. Based on this model, we developed a general-purpose MLIP for carbon that provides a robust description of the potential energy surface and accurately reproduces the physical properties of various

atomic structures. We demonstrated the performance of MLBOP in exploring the configuration space by carrying out the global structure search for clusters, calculating the phase diagram, and generating the enthalpy-volume maps of the RSS minima structures. These results show that it is possible to construct an MLIP that comprehensively covers the configuration space with a relatively small number of parameters within the formulation of the bond-order potential. We expect that MLBOP developed in this study will contribute to the discovery of new carbon materials with unique mechanical properties. In addition, the incorporation of the bond-order-based output layer with bond-embedded descriptors for more than four bodies should also be an interesting topic for future research.

DATA AVAILABILITY

The training and testing datasets listed in Table I and II are provided in Ref. [86]. The PyTorch implementation of MLBOP is provided in [86]. The input scripts, log files, and source codes of DeePMD, ACE, and SchNet for reproducing the training results are provided in Ref. [86]. The LAMMPS implementation and parameters of the bonding energy part E_{bond} and the dispersion energy correction part E_{disp} of MLBOP are available in Ref. [87] and Ref. [88], respectively. Other data and codes supporting the findings of this study are available from the contact author upon reasonable request.

ACKNOWLEDGEMENTS

We acknowledge Center for Computational Materials Science, Institute for Materials Research, Tohoku University for the facilities of MASAMUNE-IMR. Additional computing facilities were provided by Initiative on Recommendation Program for Young Researchers and Woman Researchers, Information Technology Center, The University of Tokyo. A part of this work was supported by JSPS (KAKENHI JP21KK0087, JP22H01411, JP23H00174, JP23H05443) and JST (CREST JP-MJCR20B5, SPRING JPMJSP2108).

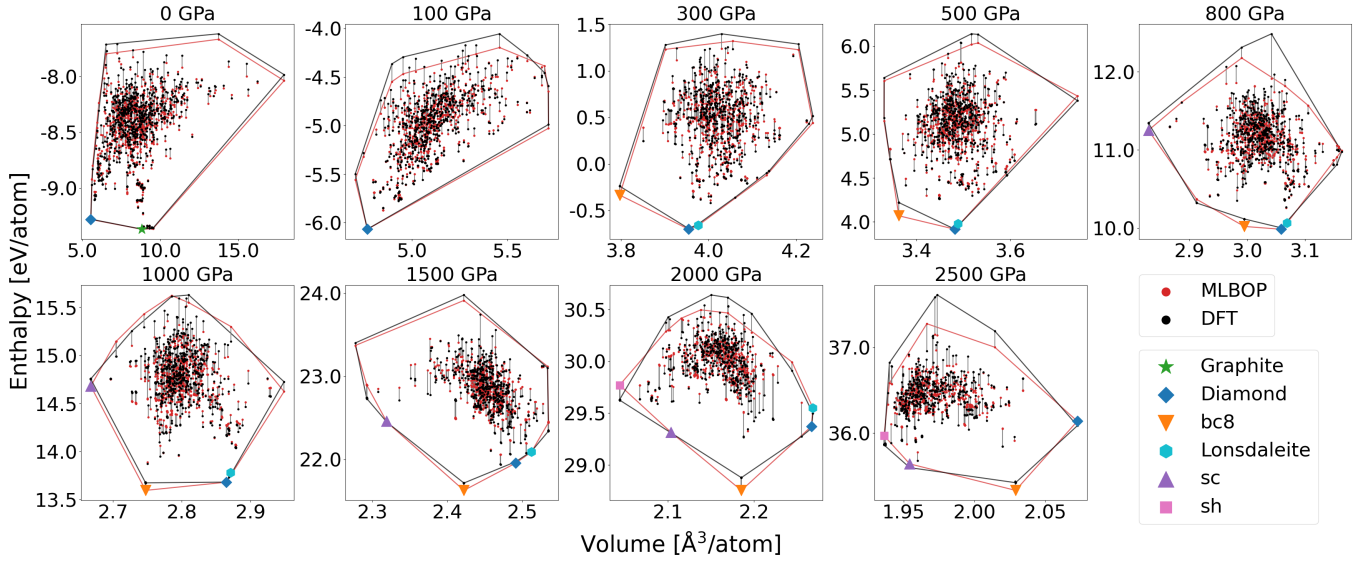


FIG. 11. Enthalpies and volumes of the MLBOP RSS minima structures at 0, 100, 300, 500, 800, 1000, 1500, 2000, and 2500 GPa. The red points indicate the MLBOP RSS minima and the black points indicate the DFT-recalculated enthalpies of the same minima structures. The red and black lines are the convex hulls surrounding the RSS minima points with the same colors. The convex hull points corresponding to AB-stacked graphite, diamond, bc8, Lonsdaleite, sc, and simple hexagonal (sh) are represented by various markers.

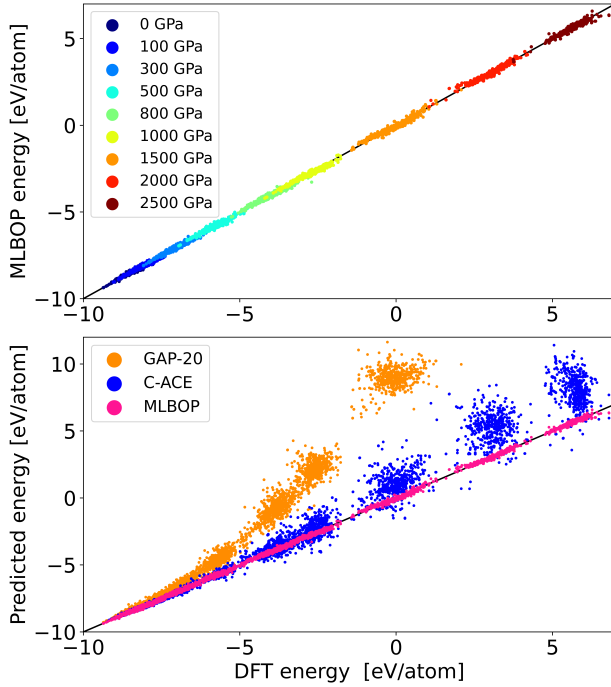


FIG. 12. Top: Comparison of the RSS minima energies between DFT and MLBOP. Bottom: Comparison of the energy prediction on the same RSS minima between GAP-20, C-ACE, and MLBOP.

-
- [1] H. W. Kroto, J. R. Heath, S. C. O'Brien, R. F. Curl, and R. E. Smalley, *Nature* **318**, 162 (1985).
- [2] K. S. Novoselov, A. K. Geim, S. V. Morozov, D. Jiang, Y. Zhang, S. V. Dubonos, I. V. Grigorieva, and A. A. Firsov, *Science* **306**, 666 (2004).
- [3] S. Iijima, *Nature* **354**, 56 (1991).
- [4] S. Iijima and T. Ichihashi, *Nature* **363**, 603 (1993).
- [5] M. Amsler, J. A. Flores-Livas, L. Lehtovaara, F. Balima, S. A. Ghasemi, D. Machon, S. Pailhès, A. Willand, D. Caliste, S. Botti, A. San Miguel, S. Goedecker, and M. A. L. Marques, *Phys. Rev. Lett.* **108**, 065501 (2012).
- [6] Q. Li, Y. Ma, A. R. Oganov, H. Wang, H. Wang, Y. Xu, T. Cui, H.-K. Mao, and G. Zou, *Phys. Rev. Lett.* **102**, 175506 (2009).
- [7] K. Umemoto, R. M. Wentzcovitch, S. Saito, and T. Miyake, *Phys. Rev. Lett.* **104**, 125504 (2010).
- [8] C. He, L. Sun, C. Zhang, X. Peng, K. Zhang, and J. Zhong, *Solid State Commun.* **152**, 1560 (2012).
- [9] G. C. Abell, *Phys. Rev. B* **31**, 6184 (1985).
- [10] J. Tersoff, *Phys. Rev. Lett.* **56**, 632 (1986).
- [11] J. Tersoff, *Phys. Rev. B* **38**, 9902 (1988).
- [12] J. Tersoff, *Phys. Rev. B* **37**, 6991 (1988).
- [13] J. Tersoff, *Phys. Rev. Lett.* **61**, 2879 (1988).
- [14] J. Tersoff, *Phys. Rev. B* **39**, 5566 (1989).
- [15] J. Tersoff, *Phys. Rev. B* **41**, 3248 (1990).
- [16] J. Tersoff, *Phys. Rev. Lett.* **64**, 1757 (1990).
- [17] D. W. Brenner, *Phys. Rev. B* **42**, 9458 (1990).
- [18] D. W. Brenner, *Phys. Rev. B* **46**, 1948 (1992).
- [19] D. W. Brenner, O. A. Shenderova, J. A. Harrison, S. J. Stuart, B. Ni, and S. B. Sinnott, *J. Phys. Condens. Matter* **14**, 783 (2002).
- [20] S. J. Stuart, A. B. Tutein, and J. A. Harrison, *J. Chem. Phys.* **112**, 6472 (2000).
- [21] J. H. Los and A. Fasolino, *Phys. Rev. B* **68**, 024107 (2003).
- [22] J. H. Los, L. M. Ghiringhelli, E. J. Meijer, and A. Fasolino, *Phys. Rev. B* **72**, 214102 (2005).
- [23] J. H. Los, L. M. Ghiringhelli, E. J. Meijer, and A. Fasolino, *Phys. Rev. B* **73**, 229901 (2006).
- [24] L. M. Ghiringhelli, J. H. Los, A. Fasolino, and E. J. Meijer, *Phys. Rev. B* **72**, 214103 (2005).
- [25] T. Kumagai, S. Izumi, S. Hara, and S. Sakai, *Comput. Mater. Sci.* **39**, 457 (2007).
- [26] L. Pastewka, P. Pou, R. Pérez, P. Gumbsch, and M. Moseler, *Phys. Rev. B* **78**, 161402 (2008).
- [27] L. Pastewka, A. Klemenz, P. Gumbsch, and M. Moseler, *Phys. Rev. B* **87**, 205410 (2013).
- [28] S. Takamoto, T. Yamasaki, J. Nara, T. Ohno, C. Kaneta, A. Hatano, and S. Izumi, *Phys. Rev. B* **97**, 125411 (2018).
- [29] K. Hisama, R. Yoshikawa, T. Matsuo, T. Noguchi, T. Kawasuzuki, S. Chiashi, and S. Maruyama, *J. Phys. Chem. C* **122**, 9648 (2018).
- [30] R. Z. Khaliullin, H. Eshet, T. D. Kühne, J. Behler, and M. Parrinello, *Phys. Rev. B* **81**, 100103 (2010).
- [31] J. Behler and M. Parrinello, *Phys. Rev. Lett.* **98**, 146401 (2007).
- [32] A. P. Bartók, M. C. Payne, R. Kondor, and G. Csányi, *Phys. Rev. Lett.* **104**, 136403 (2010).
- [33] Y. Shaidu, E. Küçükbenli, R. Lot, F. Pellegrini, E. Kaxiras, and S. de Gironcoli, *npj Comput. Mater.* **7**, 52 (2021).
- [34] D. Hedman, T. Rothe, G. Johansson, F. Sandin, J. A. Larsson, and Y. Miyamoto, *Carbon Trends* **3**, 100027 (2021).
- [35] J. Wang, H. Shen, R. Yang, K. Xie, C. Zhang, L. Chen, K.-M. Ho, C.-Z. Wang, and S. Wang, *Carbon* **186**, 1 (2022).
- [36] V. L. Deringer and G. Csányi, *Phys. Rev. B* **95**, 094203 (2017).
- [37] P. Rowe, V. L. Deringer, P. Gasparotto, G. Csányi, and A. Michaelides, *J. Chem. Phys.* **153**, 034702 (2020).
- [38] P. Rowe, V. L. Deringer, P. Gasparotto, G. Csányi, and A. Michaelides, *J. Chem. Phys.* **156**, 159901 (2022).
- [39] Y. Wang, Z. Fan, P. Qian, T. Ala-Nissila, and M. A. Caro, *Chem. Mater.* **34**, 617 (2022).
- [40] M. Qamar, M. Mrovec, Y. Lysogorskiy, A. Bochkarev, and R. Drautz, *J. Chem. Theory Comput.* **19**, 5151 (2023).
- [41] J. T. Willman, K. Nguyen-Cong, A. S. Williams, A. B. Belonoshko, S. G. Moore, A. P. Thompson, M. A. Wood, and I. I. Oleynik, *Phys. Rev. B* **106**, L180101 (2022).
- [42] V. N. Vapnik, *The nature of statistical learning theory* (Springer-Verlag, New York, 2000).
- [43] G. P. P. Pun, R. Batra, R. Ramprasad, and Y. Mishin, *Nat. Commun.* **10**, 2339 (2019).
- [44] G. P. P. Pun, V. Yamakov, J. Hickman, E. H. Glaessgen, and Y. Mishin, *Phys. Rev. Mater.* **4**, 113807 (2020).
- [45] Y.-S. Lin, G. P. P. Pun, and Y. Mishin, *Comput. Mater. Sci.* **205**, 111180 (2022).
- [46] S. Grimme, J. Antony, S. Ehrlich, and H. Krieg, *J. Chem. Phys.* **132**, 154104 (2010).
- [47] S. Grimme, S. Ehrlich, and L. Goerigk, *J. Comput. Chem.* **32**, 1456 (2011).
- [48] K. He, X. Zhang, S. Ren, and J. Sun, Delving deep into rectifiers: Surpassing human-level performance on imagenet classification (2015), arXiv:1502.01852.
- [49] D. P. Kingma and J. Ba, Adam: A Method for Stochastic Optimization (2017), arXiv:1412.6980.
- [50] J. P. Perdew, K. Burke, and M. Ernzerhof, *Phys. Rev. Lett.* **77**, 3865 (1996).
- [51] J. P. Perdew, K. Burke, and M. Ernzerhof, *Phys. Rev. Lett.* **78**, 1396 (1997).
- [52] G. Kresse and J. Hafner, *Phys. Rev. B* **47**, 558 (1993).
- [53] G. Kresse and J. Hafner, *J. Phys. Condens. Matter* **6**, 8245 (1994).
- [54] G. Kresse and J. Furthmüller, *Phys. Rev. B* **54**, 11169 (1996).
- [55] G. Kresse and D. Joubert, *Phys. Rev. B* **59**, 1758 (1999).
- [56] L. Zhang, J. Han, H. Wang, R. Car, and W. E, *Phys. Rev. Lett.* **120**, 143001 (2018).
- [57] R. Drautz, *Phys. Rev. B* **99**, 014104 (2019).
- [58] H. Wang, L. Zhang, J. Han, and W. E, *Comp. Phys. Comm.* **228**, 178 (2018).
- [59] Y. Lysogorskiy, C. v. d. Oord, A. Bochkarev, S. Menon, M. Rinaldi, T. Hammerschmidt, M. Mrovec, A. Thompson, G. Csányi, C. Ortner, *et al.*, *npj Comput. Mater.* **7**, 1 (2021).
- [60] R. Hoffmann, A. A. Kabanov, A. A. Golov, and D. M. Proserpio, *Angew. Chem. Int. Ed* **55**, 10962 (2016).
- [61] C. J. Pickard and R. J. Needs, *J. Phys. Condens. Matter* **23**, 053201 (2011).
- [62] P. E. Blöchl, *Phys. Rev. B* **50**, 17953 (1994).

- [63] K. T. Schütt, H. E. Sauceda, P.-J. Kindermans, A. Tkatchenko, and K.-R. Müller, *J. Chem. Phys.* **148**, 241722 (2018).
- [64] D. Hendrycks and K. Gimpel, Gaussian Error Linear Units (GELUs) (2023), arXiv:1606.08415.
- [65] <https://pytorch-geometric.readthedocs.io/en/latest/>.
- [66] K. Lee, E. D. Murray, L. Kong, B. I. Lundqvist, and D. C. Langreth, *Phys. Rev. B* **82**, 081101 (2010).
- [67] J. c. v. Klimeš, D. R. Bowler, and A. Michaelides, *Phys. Rev. B* **83**, 195131 (2011).
- [68] M. Dion, H. Rydberg, E. Schröder, D. C. Langreth, and B. I. Lundqvist, *Phys. Rev. Lett.* **92**, 246401 (2004).
- [69] J. Klimeš, D. R. Bowler, and A. Michaelides, *J. Phys. Condens. Matter* **22**, 022201 (2009).
- [70] A. P. Thompson, H. M. Aktulga, R. Berger, D. S. Bolinteanu, W. M. Brown, P. S. Crozier, P. J. in 't Veld, A. Kohlmeyer, S. G. Moore, T. D. Nguyen, R. Shan, M. J. Stevens, J. Tranchida, C. Trott, and S. J. Plimpton, *Comp. Phys. Comm.* **271**, 108171 (2022).
- [71] A. D. Becke, *J. Chem. Phys.* **98**, 5648 (1993).
- [72] C. Lee, W. Yang, and R. G. Parr, *Phys. Rev. B* **37**, 785 (1988).
- [73] P. J. Stephens, F. J. Devlin, C. F. Chabalowski, and M. J. Frisch, *J. Phys. Chem.* **98**, 11623 (1994).
- [74] M. D. L. Pierre, M. Bruno, C. Manfredotti, F. Nestola, M. Prencipe, and C. Manfredotti, *Mol. Phys.* **112**, 1030 (2014).
- [75] F. Li and J. S. Lannin, *Phys. Rev. Lett.* **65**, 1905 (1990).
- [76] A. Togo, L. Chaput, T. Tadano, and I. Tanaka, *J. Phys. Condens. Matter* **35**, 353001 (2023).
- [77] A. Togo, *J. Phys. Soc. Jpn.* **92**, 012001 (2023).
- [78] D. M. Deaven and K. M. Ho, *Phys. Rev. Lett.* **75**, 288 (1995).
- [79] R. O. Jones, *J. Chem. Phys.* **110**, 5189 (1999).
- [80] J. R. Morris, C. Z. Wang, K. M. Ho, and C. T. Chan, *Phys. Rev. B* **49**, 3109 (1994).
- [81] P. J. Steinhardt, D. R. Nelson, and M. Ronchetti, *Phys. Rev. B* **28**, 784 (1983).
- [82] F. Bundy, W. Bassett, M. Weathers, R. Hemley, H. Mao, and A. Goncharov, *Carbon* **34**, 141 (1996).
- [83] A. A. Correa, S. A. Bonev, and G. Galli, *Proc. Natl. Acad. Sci. USA* **103**, 1204 (2006).
- [84] G. A. Marchant, M. A. Caro, B. Karasulu, and L. B. Pártay, *npj Comput. Mater.* **9**, 131 (2023).
- [85] A. Bochkarev, Y. Lysogorskiy, S. Menon, M. Qamar, M. Mrovec, and R. Drautz, *Physical Review Materials* **6**, 013804 (2022).
- [86] The datasets and source codes are available in <https://doi.org/10.5281/zenodo.14280614>.
- [87] The LAMMPS implementation and parameters of ML-BOP are provided in https://github.com/IKOHATA/pair_mlbop.
- [88] The LAMMPS implementation of Grimme's D3 correction is provided in https://github.com/IKOHATA/pair_dftd3.